Optics Letters

Multiple-polarization-sensitive photodetector based on a perovskite metasurface

Cheng-Yao Li,[1] Chaowei Chen,[1] Yu Liu,[1] Jing Su,[2] Dong-Xiang Qi,[1] Jie He,[1] Ren-Hao Fan,[1] Qing Cai,[1] Qingxuan Li,[1] Ruwen Peng,[1,4] Xian-Rong Huang,[3,5] and Mu Wang[1,6]

[1]National Laboratory of Solid State Microstructures, School of Physics, and Collaborative Innovation Center of Advanced Microstructures, Nanjing University, Nanjing 210093, China
[2]School of Physics & Optoelectronic Engineering, Nanjing University of Information Science & Technology, Nanjing 210044, China
[3]Advanced Photon Source, Argonne National Laboratory, Argonne, Illinois 60439, USA
[4]e-mail: rwpeng@nju.edu.cn
[5]e-mail: xiahuang@anl.gov
[6]e-mail: muwang@nju.edu.cn

Received 26 August 2021; revised 17 November 2021; accepted 26 November 2021; posted 1 December 2021; published 20 January 2022

Most polarization-sensitive photodetectors detect either linearly polarized (LP) or circularly polarized (CP) light. Here, we experimentally demonstrate a multiple-polarization photodetector based on a hybrid organic–inorganic perovskite (HOIP) metasurface, which is sensitive to both LP and CP light simultaneously. The perovskite metasurface is composed of a HOIP antenna array on a single-crystal HOIP film. Owing to the antenna anisotropy, the absorption of linearly polarized light at the metasurface depends on the polarization angle; also, due to the mirror asymmetry of the antenna elements, the metasurface is also sensitive to different circular polarizations. Polarization-dependent photocurrent responses to both LP and CP light are detected. Our results highlight the potential of perovskite metasurfaces for integrated photoelectric applications.

https://doi.org/10.1364/OL.441505

Light polarization has been adapted for use in many diverse fields, including communications, optical switching, near-field imaging, and biological sensors [1–6]. There are already some electronic devices that can identify light polarization. One strategy is to use polarization-sensitive materials as active layers that can naturally detect linearly polarized (LP) or circularly polarized (CP) light. These materials can be anisotropic two-dimensional (2D) materials [7–10] or chiral organic semiconductors [11,12]. Nevertheless, the types of materials with these properties are limited. In contrast, electronic devices containing polarization-responsive metasurfaces combined with 2D materials have also been shown to be capable of detecting polarized light, with the metasurfaces providing different resonance absorption enhancements for different light polarizations [13–18]. However, these devices inevitably suffer from metal losses and are hampered by the complexity of the fabrication processes.

Hybrid organic–inorganic perovskites (HOIPs) have emerged as a class of promising semiconductors for advanced optoelectronic devices [19–22]. Polarization-responsive photodetectors based on HOIPs have also been rapidly developed in the last few years. Perovskite microcylinders and microwires with anisotropic alignment are used for LP light detection [23–26], and chiral perovskite with intrinsic CP-sensitive absorption has been exploited to detect CP light [27–31]. However, these photodetectors can only provide a single functionality, detecting either LP or CP light. Very recently, Li *et al*. reported a plasmonic metasurface integrated graphene–silicon photodetector that can achieve circular- and linear-polarization-resolved photoresponses [18]. However, the detection of LP and CP light simultaneously in a single electronic device is still rarely reported, even though it is important to achieve multiple functionality to meet the increasing demand for miniaturization and integration in optoelectronics. The advances made in perovskite metasurfaces provide a feasible platform to solve this problem. The potential of HOIPs in all-dielectric metasurfaces has recently been demonstrated. Their high refractive indices are comparable to those of conventional transparent materials [32], which offers new opportunities for fundamental physics research and optoelectronic applications, including emission enhancement [33–36], strong light–matter coupling [37], and light trapping and photon-to-electron conversion [22]. Therefore, by combining the high optical refractive index and excellent electrical characteristics of HOIPs, it should be possible to develop new devices based on HOIP metasurfaces that are capable of multiple-polarization photodetection.

In this work, we experimentally demonstrate a multiple-polarization-sensitive photodetector based on an all-dielectric HOIP metasurface that can measure both LP and CP light. A schematic of the proposed HOIP metasurface is presented in Fig. 1(a). The metasurface is composed of a periodic array of L-shaped HOIP nanoantennas on top of a HOIP thin film. Because the antenna unit of the metasurface is anisotropic in the x-axis and y-axis directions, the L-shaped HOIP metasurface is expected to respond differently to x-polarized and y-polarized electromagnetic waves. Figure 1(b) depicts the reflection and transmission spectra of the HOIP metasurface under LP light irradiation, as simulated using the finite-difference time-domain simulation software package from Lumerical Inc. The optical

constants of the HOIP used in the simulation are from Ref. [32]. There are many peaks and dips in the reflection and transmission spectra, which may originate from the Mie resonance modes and cavity modes excited in the metasurface [3,22]. Reflection at the metasurface is effectively suppressed, and differs slightly for the different types of LP light. However, from the transmission spectra, it is apparent that the metasurface transmits more x-polarized light than y-polarized light over the wavelength range of 500–750 nm. Based on the reflection and transmission data, the absorption A can be calculated using the relationship $A = 1 - R - T$, where R and T denote reflection and transmission, respectively. As depicted in Fig. 1(c), the absorption of y-polarized light at the metasurface is significantly enhanced compared to the absorption of x-polarized light in the range of 500–750 nm. To better understand the mechanism underlying the polarization sensitivity of the designed HOIP metasurface, we simulated the electric field distributions at a wavelength of 700 nm in the x–y plane under LP light excitation, as illustrated in Fig. 1(f). The electric field is distributed mainly at the edge of the short bar of the L-shaped antenna under x-polarized light irradiation, whereas the field distribution under y-polarized light irradiation is more localized around the long bar, which leads to a polarization-dependent difference in absorption.

Furthermore, our designed perovskite metasurface not only responds sensitively to LP light but can also be used for the detection of CP light due to the L-shaped chiral nanoantenna units, which break the mirror symmetry. In the simulation results shown in Fig. 1(d), we can see that the reflectivity/transmissivity of the chiral metasurface is different when CP light illuminates the structures. Consequently, the resulting absorption spectra also show selective enhancement of optical absorption for different CP light illuminations. As shown in Fig. 1(e), the metasurface can absorb more left circularly polarized (LCP) light than right circularly polarized (RCP) light around a wavelength of 650 nm. The electric field distributions in the x–y plane under LCP and RCP excitation at 650 nm are shown in Fig. 1(g). The electric field distributions of the excited resonances in the structure are clearly different, and the enhancement of the electric field for LCP illumination is stronger than that for RCP illumination at approximately 650 nm, which leads to a CP-dependent difference in the absorption spectra.

During the experiment, we first grew a single-crystal $CH_3NH_3PbI_3$ ($MAPbI_3$) film on a freshly cleaved mica substrate via a quasi-static solution growth process [38,21]. A brief schematic of the growth process is provided in Fig. 2(a). $MAPbI_3$ solution was dropped onto the freshly cleaved mica substrate and covered with another mica slice to create a confined growth space. Next, the mica–solution–mica sandwich was placed on a heater to achieve quasi-static solution growth. Finally, we obtained a uniform large-area (transverse size > 50 μm) $MAPbI_3$ film between the two pieces of mica. An optical image and an atomic force microscopy (AFM) image of the as-grown $MAPbI_3$ film are shown in Figs. 2(b) and 2(c), respectively. Figure 2(d) depicts the absorption and photoluminescence (PL) spectra of the $MAPbI_3$ film, which exhibits a bandgap of 1.6 eV and a strong PL peak at approximately 780 nm.

Then we fabricated the metasurface by etching a 170-nm-thick single-crystal $MAPbI_3$ film using a dual-beam focused ion beam (FIB) milling system (Helios, Nanolab 600i). A scanning electron microscopy (SEM) image of the $MAPbI_3$ metasurface is depicted in Fig. 3(a), where uniform L-shaped unit cells are arranged in neat rows within an area of 400 μm^2.

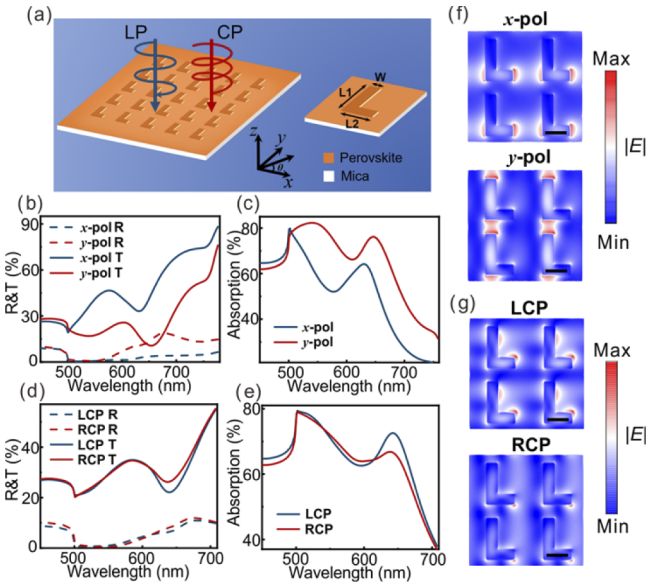

Fig. 1. The HOIP metasurface and its simulated optical response. (a) Schematic of the designed HOIP metasurface; the geometrical parameters of the unit cell are $L_1 = 380$ nm, $L_2 = 250$ nm, $W = 100$ nm, and $p = 500$ nm. The lengths of each L antenna in the x and y directions are L_2 and L_1, respectively. W and p represent the width and the periodicity, respectively. The thicknesses of each L antenna and the lower HOIP thin film are 160 nm and 10 nm, respectively. (b), (c) HOIP metasurface under incident x- and y-polarized light: (b) simulated reflection (x-polarization, lower dashed curve; y-polarization, upper dashed curve) and transmission (x-polarization, upper solid curve; y-polarization, lower solid curve) and (c) simulated absorption spectra (x-polarization, lower solid curve; y-polarization, upper solid curve). (d), (e) HOIP metasurface under incident LCP and RCP light: (d) simulated reflection (LCP, lower dashed curve; RCP, upper dashed curve) and transmission (LCP, lower solid curve; RCP, upper solid curve) and (e) simulated absorption spectra (LCP, upper solid curve; RCP, lower solid curve). (f), (g) Simulated electric field distributions (f) under incident x- and y-polarized light at a wavelength of 700 nm and (g) under incident LCP and RCP light at a wavelength of 650 nm; the scale bars indicate 200 nm.

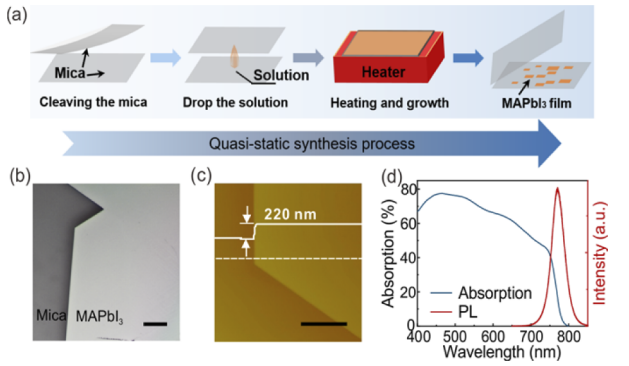

Fig. 2. HOIP ($MAPbI_3$) films. (a) Schematic of the quasi-static solution growth process. (b) Optical microscopy image. (c) AFM image. (d) Absorption (left curve) and PL (right curve) spectra. The scale bars indicate 10 μm.

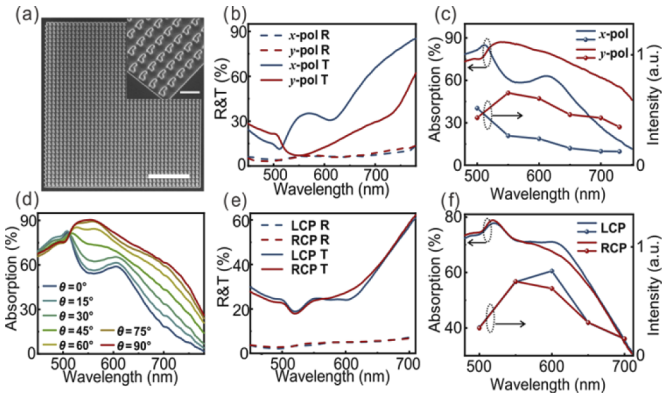

Fig. 3. Experimentally measured optical spectra. (a) SEM images of the $MAPbI_3$ metasurface; the scale bar indicates 5 μm. Inset: SEM image tilted at 30°; the scale bar indicates 500 nm. (b), (e) Reflection and transmission spectra under (b) incident LP light [line description is the same as in Fig. 1(b)] and (e) CP light [line description is the same as in Fig. 1(d)]. (c), (f) Absorption and PLE spectra under (c) incident LP light (*x*-polarization, lower solid curve; *y*-polarization, upper solid curve) and (f) CP light (LCP, upper solid curve; RCP, lower solid curve). (d) The absorption of LP light with different polarization angles (from top to bottom, 90°, 75°, 60°, 45°, 30°, 15°, 0°.

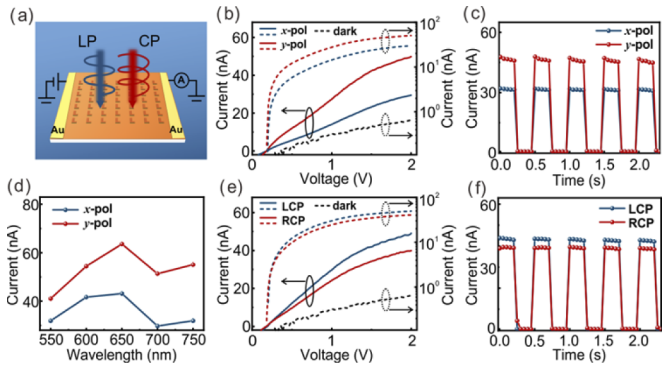

Fig. 4. Electrical characteristics of the metasurface. (a) Measurement setup used for the electrical measurements. (b), (e) Measured *I–V* curves under (b) LP light illumination (*x*-polarization, lower dashed curve; *y*-polarization, upper dashed curve) and (e) CP light illumination (LCP, upper dashed curve; RCP, lower dashed curve). The data associated with the left axis are $I_{light} - I_{dark}$ values on a linear scale, and the data associated with the right axis are values of the currents I_{light} and I_{dark} on a logarithmic scale. (c), (f) Time-resolved photocurrents of the device under (c) periodic on/off LP light illumination (*x*-polarization, lower curve; *y*-polarization, upper curve) and (f) CP light illumination (LCP, upper curve; RCP, lower curve). (d) Measured photocurrents of the metasurface with incident LP light of different excitation wavelengths (*x*-polarization, lower solid curve; *y*-polarization, upper solid curve).

The inset in Fig. 3(a) is an SEM image of the metasurface tilted at 30°; the etching depth was approximately 160 nm. The unetched bottom film supports the carrier transport. As shown in Figs. 3(b) and 3(e), we measured the reflection and transmission spectra of the HOIP metasurface under LP and CP light illumination using an ultraviolet–visible–near-infrared microspectrophotometer (CRAIC, QDI2010). The absorption spectra shown in Figs. 3(c) and 3(f) were obtained, and are reasonably consistent with the simulated results shown in Fig. 1. All the above data (R, T, A) were obtained from one sample. The minor difference between the experimental and simulation results may be due to the tolerances of the experimental parameters during the fabrication processes. The absorption at the metasurface under *y*-polarized light illumination is more than that under *x*-polarized light illumination in the range of 550–750 nm, and increases as the polarization angle increases, as shown in Fig. 3(d). In the wavelength range of 550–750 nm, the absorption has a minimum when the polarization angle of the incident light is 0° ($\theta = 0°$), but the absorption changes with the polarization angle, reaching its maximum at a polarization angle of 90° ($\theta = 90°$). θ is the angle between the direction of LP light and the *x*-axis, as shown in Fig. 1(a). Furthermore, we find that the absorption of LCP differs from the absorption of RCP light by the metasurface around a wavelength of 610 nm. In Figs. 3(c) and 3(f), we present photoluminescence excitation (PLE) spectra, which agree reasonably well with the measured absorption data. Note that the absorption of the HOIP metasurface could be further increased by improving the metasurface design, such as by introducing a Fabry–Perot cavity.

It was confirmed above that a perovskite metasurface can produce different resonance modes that have different field localized effects depending on the type of polarized light that excites the metasurface. Logically, changing the type of polarized light absorbed could change the number of photoinduced carriers generated, leading to different photocurrent responses for different types of polarized light. A schematic of the electrical measurement setup is shown in Fig. 4(a). A pair of gold electrodes were deposited on both sides of the metasurface using electron-beam evaporation. Then we used a source meter (Keithley Instruments, 2636 B) to apply bias voltages and detect the current signals. A continuous-wave laser with a spot size of about 100 μm^2 and a stable power of 10 μW was focused on the sample to generate charge carriers. The photocurrent is expressed as $I = I_{light} - I_{dark}$, where I_{light} and I_{dark} represent the measured current values with and without illumination, respectively.

We first consider the case of LP light excitation. Figure 4(b) shows the measured *I–V* curves under *x*- and *y*-polarized 700 nm laser illumination. As the voltage changed from 0 to 2 V, the photocurrents generated under *y*-polarized light illumination were always higher than that generated under *x*-polarized light illumination. In addition, it should be noted that when the metasurface was illuminated with different wavelengths ranging from 550 to 750 nm, the photocurrents obtained under *y*-polarized light excitation were obviously higher than those obtained under *x*-polarized light irradiation, which indicates the capacity of the metasurface for broadband LP light detection, as shown in Fig. 4(d). The photocurrent responses of the device under CP light illumination at a wavelength of 610 nm were also measured. The *I–V* curves measured under LCP and RCP light illumination are shown in Fig. 4(e). The photocurrents generated by LCP light illumination are higher than those generated by RCP light illumination, which is consistent with the absorption spectra shown in Fig. 3(f). We find that the absorption of LCP light is not significantly different from that of RCP light, possibly because of the intrinsic absorption of HOIP; however, the difference in photocurrent response is still obvious. Interestingly, we can distinguish the photocurrent responses for 45° LP light and CP light by performing in-plane rotation of the metasurface. In addition, based on the photocurrents and dark currents obtained

under y-polarized light illumination in Fig. 4(b), we estimated the responsivity and detectivity of the device to be up to 5 mA/W and 1.1×10^8 Jones, respectively. This responsivity is higher than those of many plasmonic metasurface integrated photodetectors [13,15,16]. It should be noted that the responsivity and detectivity of a detector with a shorter channel length (approximately 5 μm) is greatly improved to 0.3 A/W and 3×10^{10} Jones, respectively, due to the shorter transport distance of photoinduced carriers. Figures 4(c) and 4(f) show the time-resolved photocurrent responses measured under 2 Hz modulated illumination by LP and CP light with a bias voltage of 2 V. During these measurements, the incident light was periodically switched on and off, and stable discrimination of the photocurrents was observed when the laser was turned on. Rise and fall times of about 40 ms and 42 ms, respectively, can be estimated from the data under x-polarized light illumination in Fig. 4(c). However, the actual response time of our device might be much faster than this value. We measured rise and fall times of about 15 μs and 12 μs, respectively, under 8 kHz modulated illumination. These results indicate that our device presents good performance in terms of LP and CP selectivity in time-sensitive applications.

In conclusion, we designed and experimentally demonstrated a multiple-polarization-sensitive photodetector based on a HOIP metasurface that detects both LP and CP light simultaneously. Our study reveals the potential of the HOIP metasurface to achieve highly efficient polarized photoelectric detection. It is expected to achieve applications in biosensing, polarization imaging, and other integrated photoelectric nanodevices.

Funding. National Key Research and Development Program of China (2020YFA0211300, 2017YFA0303702); National Natural Science Foundation of China (11634005, 61975078, 11974177); U.S. Department of Energy, Office of Science, Office of Basic Energy Sciences (DE-AC02-06CH11357).

Acknowledgment. X.-R.H. was supported by the U.S. Department of Energy, Office of Science, Office of Basic Energy Sciences (DE-AC02-06CH11357).

Disclosures. The authors declare no conflicts of interest.

Data availability. Data underlying the results presented in this paper are not publicly available at this time but may be obtained from the authors upon reasonable request.

REFERENCES

1. M. S. Long, A. Y. Gao, P. Wang, H. Xia, C. Ott, C. Pan, Y. J. Fu, E. F. Liu, X. S. Chen, W. Lu, T. Nilges, J. B. Xu, X. M. Wang, W. D. Hu, and F. Miao, Sci. Adv. **3**, e1700589 (2017).
2. M. J. Grzybowski, P. Wadley, K. W. Edmonds, R. Beardsley, V. Hills, R. P. Campion, B. L. Gallagher, J. S. Chauhan, V. Novak, T. Jungwirth, F. Maccherozzi, and S. S. Dhesi, Phys. Rev. Lett. **118**, 057701 (2017).
3. S.-C. Jiang, X. Xiong, Y. S. Hu, Y. H. Hu, G. B. Ma, R.-W. Peng, C. Sun, and M. Wang, Phys. Rev. X **4**, 021026 (2014).
4. S. Shuvaev, E. A. Suturina, K. Mason, and D. Parker, Chem. Sci. **9**, 2996 (2018).
5. J. S. Tyo, D. L. Goldstein, D. B. Chenault, and J. A. Shaw, Appl. Opt. **45**, 5453 (2006).
6. Y.-J. Gao, X. Xiong, Z. Wang, F. Chen, R.-W. Peng, and M. Wang, Phys. Rev. X **10**, 031035 (2020).
7. H. T. Yuan, X. G. Liu, F. Afshinmanesh, W. Li, G. Xu, J. Sun, B. Lian, A. G. Curto, G. J. Ye, Y. Hikita, Z. X. Shen, S.-C. Zhang, X. H. Chen, M. Brongersma, H. Y. Hwang, and Y. Cui, Nat. Nanotechnol. **10**, 707 (2015).
8. F. C. Liu, S. J. Zheng, X. X. He, A. Chaturvedi, J. F. He, W. L. Chow, T. R. Mion, X. L. Wang, J. D. Zhou, Q. D. Fu, H. J. Fan, B. K. Tay, L. Song, R.-H. He, C. Kloc, P. M. Ajayan, and Z. Liu, Adv. Funct. Mater. **26**, 1169 (2016).
9. L. Ye, P. Wang, W. J. Luo, F. Gong, L. Liao, T. D. Liu, L. Tong, J. F. Zang, J. B. Xu, and W. D. Hu, Nano Energy **37**, 53 (2017).
10. T. Hong, B. Chamlagain, W. Z. Lin, H.-J. Chuang, M. H. Pan, Z. X. Zhou, and Y.-Q. Xu, Nanoscale **6**, 8978 (2014).
11. B. J. Gilot, R. Abbel, G. Lakhwani, E. W. Meijer, A. P. H. J. Schenning, and S. C. J. Meskers, Adv. Mater. **22**, E131 (2010).
12. Y. Yang, R. C. D. Costa, M. J. Fuchter, and A. J. Campbell, Nat. Photonics **7**, 634 (2013).
13. P. K. Venuthurumilli, P. D. Ye, and X. F. Xu, ACS Nano **12**, 4861 (2018).
14. S. Chen, R. Cao, X. Chen, Q. Wu, Y. H. Zeng, S. Gao, Z. N. Guo, J. L. Zhao, M. Zhang, and H. Zhang, Adv. Mater. Interfaces **7**, 1902179 (2020).
15. W. Li, Z. J. Coppens, L. V. Besteiro, W. Y. Wang, A. O. Govorov, and J. Valentine, Nat. Commun. **6**, 8379 (2015).
16. Q. Jiang, B. W. Du, M. L. Jiang, D. L. Liu, Z. X. Liu, B. W. Li, Z. Liu, F. Lin, X. Zhu, and Z. Y. Fang, Nanoscale **12**, 5906 (2020).
17. Z. Chen, S. Chen, Y. Wang, and L. Xiao, Nanophotonics **8**, 1739 (2019).
18. L. Li, J. Wang, L. Kang, W. Liu, L. Yu, B. Zheng, M. L. Brongersma, D. H. Werner, S. Lan, Y. Shi, Y. Xu, and X. Wang, ACS Nano **14**, 16634 (2020).
19. B. R. Sutherland and E. H. Sargent, Nat. Photonics **10**, 295 (2016).
20. M. A. Green, A. Ho-Baillie, and H. J. Snaith, Nat. Photonics **8**, 506 (2014).
21. H. Jing, R. W. Peng, R.-M. Ma, J. He, Y. Zhou, Z. Q. Yang, C.-Y. Li, Y. Liu, X. J. Guo, Y. Y. Zhu, D. Wang, J. Su, C. Sun, W. Z. Bao, and M. Wang, Nano Lett. **20**, 7144 (2020).
22. H. Jing, Y. Y. Zhu, R.-W. Peng, C.-Y. Li, B. Xiong, Z. Wang, Y. Liu, and M. Wang, Nanophotonics **9**, 3323 (2020).
23. S. Lim, M. Ha, Y. Lee, and H. Ko, Adv. Opt. Mater. **6**, 1800615 (2018).
24. L. Gao, K. Zeng, J. S. Guo, C. Ge, J. Du, Y. Zhao, C. Chen, H. Deng, Y. He, H. S. Song, G. D. Niu, and J. Tang, Nano Lett. **16**, 7446 (2016).
25. J. G. Feng, X. X. Yan, Y. Liu, H. F. Gao, Y. C. Wu, B. Su, and L. Jiang, Adv. Mater. **29**, 1605993 (2017).
26. S.-X. Li, G.-P. Zhang, H. Xia, Y.-S. Xu, C. Lv, and H.-B. Sun, Nanoscale **11**, 18272 (2019).
27. C. Chen, L. Gao, W. R. Gao, C. Ge, X. Y. Du, Z. Li, Y. Yang, G. D. Niu, and J. Tang, Nat. Commun. **10**, 1927 (2019).
28. A. Ishii and T. Miyasaka, Sci. Adv. **6**, eabd3274 (2020).
29. D. Li, X. T. Liu, W. T. Wu, Y. Peng, S. G. Zhao, L. N. Li, M. C. Hong, and J. H. Luo, Angew. Chem., Int. Ed. **60**, 8415 (2021).
30. J. Wang, C. Fang, J. Q. Ma, S. Wang, L. Jin, W. C. Li, and D. H. Li, ACS Nano **13**, 9473 (2019).
31. G. Long, R. Sabatini, M. I. Saidaminov, G. Lakhwani, A. Rasmita, X. Liu, E. H. Sargent, and W. Gao, Nat. Rev. Mater. **5**, 423 (2020).
32. M. A. Green, Y. Jiang, A. M. Soufiani, and A. W.-Y. Ho-Baillie, J. Phys. Chem. Lett. **6**, 4774 (2015).
33. Y. B. Fan, Y. H. Wang, N. Zhang, W. Z. Sun, Y. S. Gao, C.-W. Qiu, Q. H. Song, and S. M. Xiao, Nat. Commun. **10**, 2085 (2019).
34. S. V. Makarov, V. Milichko, E. V. Ushakova, M. Omelyanovich, A. C. Pasaran, R. Haroldson, B. Balachandran, H. L. Wang, W. Hu, Y. S. Kivshar, and A. A. Zakhidov, ACS Photonics **4**, 728 (2017).
35. A. Kessel, C. Frydendahl, S. R. K. C. Indukuri, N. Mazurski, P. Arora, and U. Levy, Adv. Opt. Mater. **8**, 2001627 (2020).
36. H. L. Wang, S.-C. Liu, B. Balachandran, J. Moon, R. Haroldson, Z. T. Li, A. Ishteev, Q. Gu, W. D. Zhou, A. Zakhidov, and W. Hu, Opt. Express **25**, A1162 (2017).
37. N. H. M. Dang, D. Gerace, E. Drouard, G. Trippé-Allard, F. Lédée, R. Mazurczyk, E. Deleporte, C. Seassal, and H. S. Nguyen, Nano Lett. **20**, 2113 (2020).
38. B. B. Zhang, Y.-Y. Weng, X.-P. Huang, M. Wang, R.-W. Peng, N.-B. Ming, B. J. Yang, N. Lu, and L. F. Chi, Adv. Mater. **21**, 3576 (2009).